RSC Advances

ROYAL SOCIETY OF CHEMISTRY

PAPER

View Article Online
View Journal | View Issue

Cite this: *RSC Adv.*, 2026, **16**, 1863

Hydroxyethyl cellulose-based $ZnCe_{0.3}Ti_{0.7}O_3$ nanocomposites for sustainable applications in supercapacitors and hydrogen peroxide sensors

Ali B. Abou Hammad,*[a] Amany M. El Nahrawy,*[a] Hend S. Magar[b] and Samir Kamel[c]

We report the fabrication of multifunctional nanocomposites *via* integrating $ZnCe_{0.3}Ti_{0.7}O_3$ nanoparticles into a hydroxyethyl cellulose (HEC)-based matrix to enhance electrical, charge storage, and sensing capabilities for sustainable energy, electronics, and biosensing applications. The dielectric and conductivity behaviors of the HEC@$ZnCe_{0.3}Ti_{0.7}O_3$ composites were investigated over a broad frequency (4 Hz–8 MHz) and temperature range (30–140 °C). Results showed a considerable increase in the dielectric constant at low frequencies due to interfacial and dipolar polarization, with higher values achieved upon nanoparticle incorporation. Relaxation peaks in the loss tangent shifted with temperature, indicating thermally activated dipolar processes. Composites with 1.5–3 wt% $ZnCe_{0.3}Ti_{0.7}O_3$ exhibited superior conductivity, attributed to enhanced ionic conduction pathways. Electrochemical analysis demonstrated strong pseudocapacitive behavior and rapid electron transfer. The optimized (S2) nanocomposite exhibited exceptional sensitivity for non-enzymatic hydrogen peroxide detection, with a wider linear range (0.05–2000 μM), higher sensitivity (0.998 μA μM^{-1}), and a low detection border of 0.02 μM. These results highlight the potential of HEC-based $ZnCe_{0.3}Ti_{0.7}O_3$ nanocomposites for high-performance energy storage, optoelectronic, and sensing devices.

Received 9th November 2025
Accepted 23rd December 2025

DOI: 10.1039/d5ra08647g

rsc.li/rsc-advances

Introduction

Hybrid inorganic–organic nanocomposites characterize an emerging class of functional nanomaterials that display chemical stability, and enhanced conductive, electrochemical, and mechanical properties.[1–5] These improvements arise from the synergistic physical and chemical interactions between their inorganic and organic constituents. Cellulose is one of the most abundant biopolymers globally. It constitutes the structural component of plant cell walls. It is a polysaccharide macromolecule consisting of glucose units through D-pyranosyl glucose β-glycoside bonding, and it is insoluble in water because of its higher crystallinity.[1,6,7] The various forms and derivatives of cellulose have been extensively studied. Natural cellulose has served as a foundational material in the development of polymer matrix nanocomposites reinforced with mineral nanoparticles, metal nanoparticles, and nanofibers, as well as in hybrid nanocomposites.[8,9]

According to the unique properties of cellulose and its derivatives, electrochemical sensors based on cellulose are particularly noteworthy. They show a notable role in medical diagnostic tools, environmental nursing, food safety applications, and forensic science.[10–12] Various methods have been utilized to improve the electrochemical sensors based on cellulose matrices. Techniques initially designed for nanocomposite production have been adapted to enhance sensitivity, enabling the creation of cellulose materials engineered explicitly for electrochemical detection.[13,14]

One of the attractive cellulose ether derivatives is the hydroxyethyl cellulose (HEC), which is a partially substituted polyhydroxyethyl ether of cellulose. Compared to other cellulose derivatives, its chain contains a massive number of –OH groups. It is a non-ionic, renewable, water-soluble cellulose derivative with excellent capabilities as a binding, thickening, dispersing, and emulsifying agent.[15] HEC plays a versatile role in electrochemical sensing due to its unique structural and physicochemical properties. It can act as a biocompatible polymer matrix that uniformly disperses electroactive nanoparticles.[16,17] Also, it facilitates the stability of immobilization of electroactive nanoparticles on electrode surfaces without agglomeration. HEC provides strong adhesion to the electrode, improving durability during repeated measurements and thereby enhancing reproducibility.[18] Also, – OH and $-CH_2CH_3$ groups facilitate ion transport, enabling rapid electron transfer during

[a]*Solid State Physics Department, Physics Research Institute, National Research Centre, 33 El Bohouth St., Dokki, Giza, 12622, Egypt. E-mail: amany_physics_1980@yahoo.com; abohmad2@yahoo.com*

[b]*Applied Organic Chemistry Department, National Research Centre (NRC), 33 El-Bohouth St., Dokki, Cairo, 12622, Egypt*

[c]*Cellulose and Paper Department, National Research Center, Dokki, Egypt*

electrochemical reactions and increasing permeability and ionic conductivity. Additionally, the hydrophilic nature of HEC allows H_2O_2 to diffuse efficiently to the sensing interface. For example, a combination of $ZnCeTiO_3$ with HEC enables sensitive, robust, and selective sensing platforms, accepted suitability for environmental and biomedical monitoring.[18,19]

A tricarboxylic acid such as citric acid (CA) is a highly competitive natural crosslinker due to its unique properties, including non-toxicity, easy availability, strong reactivity, and the ability to bind all carbohydrates. Under heating and dry conditions, CA will expose its –COOH group, forming anhydride CA for cross-linking reaction. The –OH group of HEC will form a covalent ester bond with the CA anhydride. Because one CA molecule has three –COOH groups, three ester bonds can be formed when CA reacts with HEC. This cross-linking reaction can effectively strengthen the rigidity of the CA cross-linked HEC network.[18,20] Thus, over the past three decades, research and development of functional biomaterials cross-linked with CA has flourished. Recently, Sotolářová *et al*.[1718] have shown that coating a carbon electrode with HEC crosslinked by CA exhibited stripping voltammetry peaks. On the other hand, hydrogen peroxide (H_2O_2) is a commonly studied analyte due to its strong oxidizing properties and its widespread use in various household and industrial products, including cosmetics, dyes, disinfectants, lacquers, and shampoos. It is also a natural byproduct of enzymatic reactions catalyzed by oxidases.[21,22] Elevated concentrations of H_2O_2 in biological systems are closely related to oxidative pressure, which is implicated in the pathogenesis of several grave diseases such as Parkinson's, diabetes, Alzheimer's, Huntington's, cancer, and general disruptions in cellular homeostasis. Its detection is typically carried out using an electrochemical sensor,[23–25] colorimetric and fluorescence-based techniques.[26] Among these, electrochemical methods have gained important attention because of their simplicity, speedy response, cost-effectiveness, high sensitivity, and suitability for real-time monitoring.[26–28] In particular, non-enzymatic electrochemical sensors offer a promising alternative by overcoming the inherent limitations of enzyme-based systems, such as instability and high cost.[3,29,30] According to the literature review, to date, no studies have reported the use of $ZnCe_{0.3}Ti_{0.7}O_3$-modified electrodes for non-enzymatic hydrogen peroxide sensing. Consequently, this work aims to develop and investigate the dielectric and conductivity of HEC-loaded $ZnCe_{0.3}Ti_{0.7}O_3$. The nanoparticle $ZnCe_{0.3}Ti_{0.7}O_3$ was first prepared *via* the sol–gel method, and the prepared nanocomposites were investigated for dual functionality in energy storage and sensing applications. This study evaluates the electrochemical performance of the HEC@$ZnCe_{0.3}Ti_{0.7}O_3$ nanocomposite as a supercapacitor electrode and its sensitivity for detecting hydrogen peroxide.

Materials and methods

Materials

Hydroxyethyl cellulose (HEC) (viscosity 90–160 cP), titanium isopropoxide; $Ti(OCH(CH_3)_2)_4$, zinc acetate [$(CH_3COO)_2Zn$], acetylacetone, cerium(III) nitrate hexahydrate ($Ce(NO_3)_3\cdot 6H_2O$), Potassium ferri/ferrocyanide, hydrogen peroxide from Za-chem USA, and potassium chloride were purchased from Sigma-Aldrich with purity exceeding 99.2%. All chemicals were used without further purification.

Methods

Synthesis of $ZnCe_{0.3}Ti_{0.7}O_3$ nanoparticles. The $ZnCe_{0.3}Ti_{0.7}O_3$ nanoparticles (NPs) were synthesized *via* a sol–gel method using high-purity reagents. The sol–gel process was initiated by dissolving precise quantities of (10 mol) titanium isopropoxide in (50 mL) acetylacetone under magnetic stirring to form a transparent TiO_2 sol.

For zinc acetate and cerium nitrate, sols were prepared by dissolving 1.11 g of $(CH_3COO)_2Zn$ and 0.78 g $Ce(NO_3)_3\cdot 6H_2O$ in 40 mL H_2O and an aqueous solution of citric acid. Separately, the TiO_2 sol was dissolved in acetylacetone before mixing with the other sources to stabilize the precursors.

Then, the TiO_2 sol was mixed gradually with (Zn–Ce) solution under magnetic stirring for 30 min, followed by the addition of two drops of nitric acid to adjust the pH value of the solution to 3. The mixture was continuously stirred magnetically for another 60 min to ensure homogeneity at 60 °C. The resulting $ZnCe_{0.3}Ti_{0.7}O_3$ sol was then dried on a hotplate at 150 °C until a xerogel formed. This xerogel was subsequently calcined at 600 °C for 3 h to obtain the final $ZnCe_{0.3}Ti_{0.7}O_3$ NPs, which were well-ground before loading the polymeric matrix.

Synthesis of HEC@ $ZnCe_{0.3}Ti_{0.7}O_3$NPs nanocomposites. 2 g Hydroxyethyl cellulose (HEC) was added to 50 mL of distilled water and stirred. 0.025 g of citric acid and 0.2 mL of glycerol were added to the solution, which was stirred under moderate conditions at 40 °C. Different weights of the aqueous suspension of nanoparticles, after being sonicated, were added to the above mixture. The solution was stirred for another 2 h and then poured onto a Teflon casting plate. It was then dried in a 50 °C oven until fully dry, peeled off, and sealed in a plastic container for further testing. The $ZnCe_{0.3}Ti_{0.7}O_3$ was added to the HEC solution in ratios of 0.0, 0.5, 1.0, 1.5, and 3.0% (w/w) relative to HEC, and the samples were coded as S1, S2, S3, S4, and S5, respectively.

Characterization

- The crystalline phases of the HEC@$ZnCe_{0.3}Ti_{0.7}O_3$ nanocomposites were classified using (X-ray Bruker D8, XRD, advanced diffractometer Japan) by a monochromatized (CuKα) radiation of wavelength ($\lambda = 1.54056$ Å), working at (40 mA and 40 kV).
- The morphology is estimated using a scanning electron microscope (SEM) using a JEOL JEM-2100, Japan, at 100k× magnification and an acceleration voltage of 120 kV. The elemental distribution of $ZnCe_{0.3}Ti_{0.7}O_3$ was studied using the nondestructive energy dispersive X-ray (EDX) unit attached to the SEM.
- UV-absorbance spectra were recorded on a Shimadzu model UV-240 spectrophotometer (Shimadzu, Tokyo, Japan) at UV ($\lambda_{range} = 200:400$ nm).
- The dielectric properties, dielectric constant, loss tangent, and ac conductivity, were estimated through measuring the capacitance C_p, dielectric loss tangent (tan(δ)), and resistance R_p

of the films. A Hioki LCR meter (IM3536) was employed to perform the dielectric measurements using a two-parallel-conducting-electrode cell with a surface area of 0.29 cm^2. The measurements were documented over the frequency range from 4 Hz to 8 MHz.

Modification of screen-printed electrodes (SPEs) with a nanocomposite

Electrochemical measurements were performed using a CHI potentiostat with screen-printed electrodes (SPEs). Screen-printed electrodes (SPEs) are widely used in electrochemical sensing due to their rapid response time, low power requirements, high sensitivity, and ability to operate at room temperature. To modify the working electrode surface with synthesized nanocomposites, 10 mg of the nanocomposites were dispersed in 1 mL of double-distilled water and sonicated for 1 h to obtain a homogeneous suspension. Subsequently, 10 μL of this suspension was drop-cast onto the working electrode surface and allowed to dry, as illustrated in Fig. 1.

Electrochemical studies

For electrochemical characterization, potassium ferri/ferrocyanide and potassium chloride were used as redox and supporting electrolytes, respectively. Electrochemical impedance spectroscopy (EIS) and cyclic voltammetry (CV) were carried out using screen-printed electrodes (SPEs) modified with the synthesized nanocomposite, connected to a CHI electrochemical workstation. The SPEs, sourced from Zensors Company, measured 50 × 13 mm (height × width) and comprised three components: a silver reference electrode, a counter electrode, and a carbon-based working electrode modified with a nanocomposite. Characterization was performed in an electrolyte solution containing 0.1 M KCl and 5 mM $[Fe(CN)_6]^{3-/4-}$. Cyclic voltammetry was conducted over a potential range of −0.6 to +1.0 V at a scan rate of 0.05 V s^{-1}. EIS measurements were taken at open circuit potential with 10 mV AC amplitude across a frequency range of 10^5 to 0.1 Hz. To extract parameters such as charge transfer resistance (R_{ct}) and capacitance (C), Nyquist plots obtained from EIS data were fitted using an appropriate equivalent circuit model. Chronoamperometric analysis was performed in phosphate buffer solution (0.1 M, pH 7.0) with varying concentrations of hydrogen peroxide, using an applied potential of 0.7 V. All experimental studies carried out at room temperature.

Results and discussion

XRD study

To investigate the crystallization behavior and differences in crystallinity during the polymerization process, X-ray diffraction (XRD) analyses of HEC-based nanocomposites filled with various contents of (1–4 wt%) $ZnCe_{0.3}Ti_{0.7}O_3$ were conducted, as presented in Fig. 2. This figure shows the X-ray diffraction patterns of the $ZnCe_{0.3}Ti_{0.7}O_3$-loaded into HEC, which were dried at 50 °C, within the scanning range of $5° \leq 2\theta \leq 80°$. Fig. 2 (S1) displays the X-ray diffractogram of neat HEC. The spectrum of HEC (S1) displays two halos with intensity maxima located at $2\theta = 20.32°$ and 41.15°. This reflection indicates the crystalline behavior of the undoped polymer.[31] Upon introducing $ZnCe_{0.3}Ti_{0.7}O_3$ NPs into the HCE matrix, forming a homogeneous gel with the appearance of some XRD peaks through the polymeric matrix, and lowering the broad hump intensity at around 20.32°.

The XRD pattern of the HEC@$ZnCe_{0.3}Ti_{0.7}O_3$ nanocomposites exhibits distinct diffraction peaks located at approximately $2\theta = 20°$, 23.7°, 25.57°, 32.7°, and 53.8°. These reflections can be indexed to the crystalline phases of $ZnTiO_3$ (JCPDS: 01-085-0547) and Ce_2Zn_{17} (JCPDS: 00-029-0404), confirming the successful formation of the hybrid HEC@$ZnCe_{0.3}Ti_{0.7}O_3$ nanocomposite.

This finding provides evidence for the incorporation of $ZnCe_{0.3}Ti_{0.7}O_3$ NPs within the polymer matrix. It is also noticeable that as the content of $ZnCe_{0.3}Ti_{0.7}O_3$ NPs increases, the intensity of the diffraction peaks corresponding to the HEC membrane at $2\theta = 21.7°$ decreases. This behavior suggests

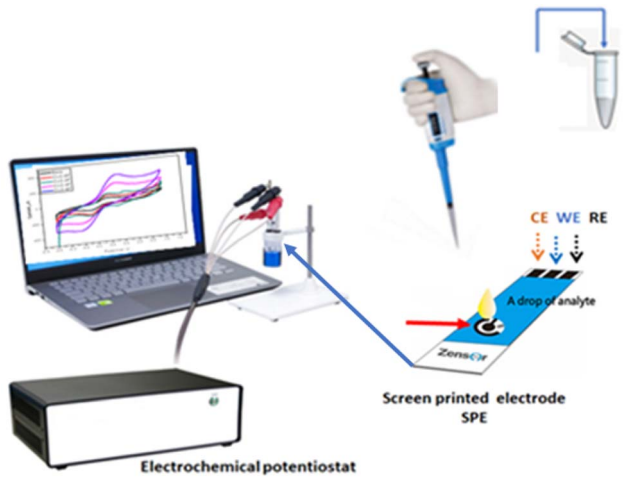

Fig. 1 Preparation of modified SPE and electrochemical detection method.

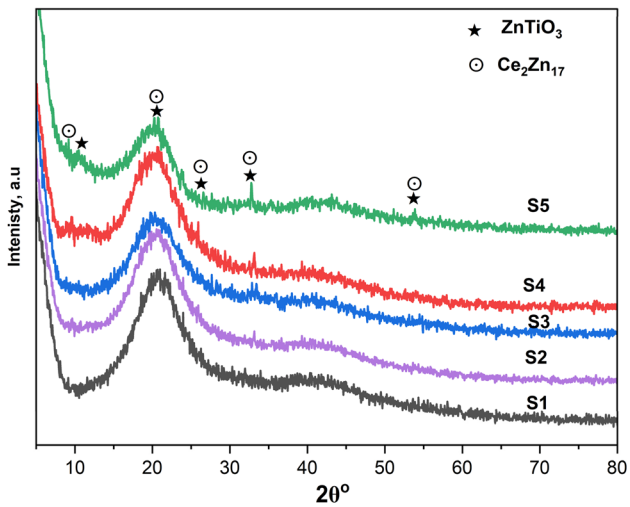

Fig. 2 XRD patterns of HEC (S1) and HEC@ $ZnCe_{0.3}Ti_{0.7}O_3$ nanocomposites (S3, S4, and S5).

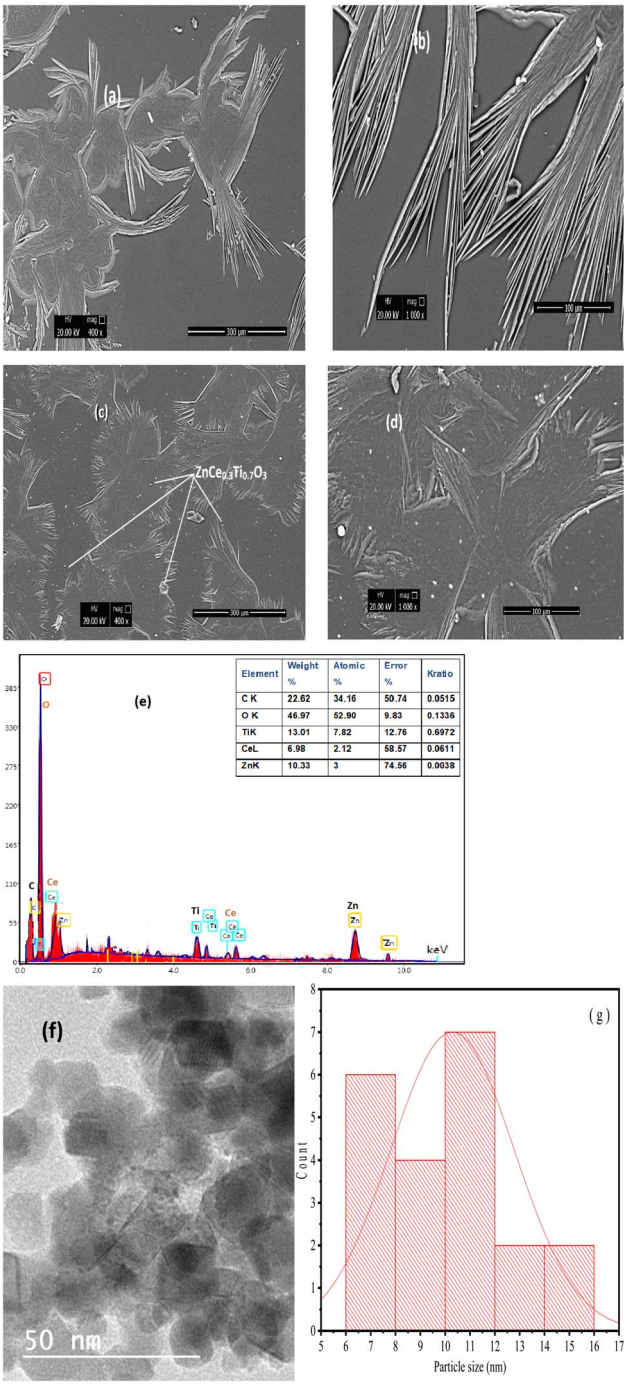

Fig. 3 SEM images (a–d) of HEC (S1) and HEC@$ZnCe_{0.3}Ti_{0.7}O_3$-nanocomposite (S3), (e) EDX pf sample S3, (f) TEM imag of S3, and (g) is the particle distribution of $ZnCe_{0.3}Ti_{0.7}O_3$ NPs.

integration and chemical interactions between the $ZnCe_{0.3}Ti_{0.7}O_3$ NPs and the HEC.

Morphological studies

The composition and surface morphology of the HEC chains and that of the $ZnCe_{0.3}Ti_{0.7}O_3$ were analyzed using energy-dispersive X-ray (EDX) spectroscopy and scanning electron

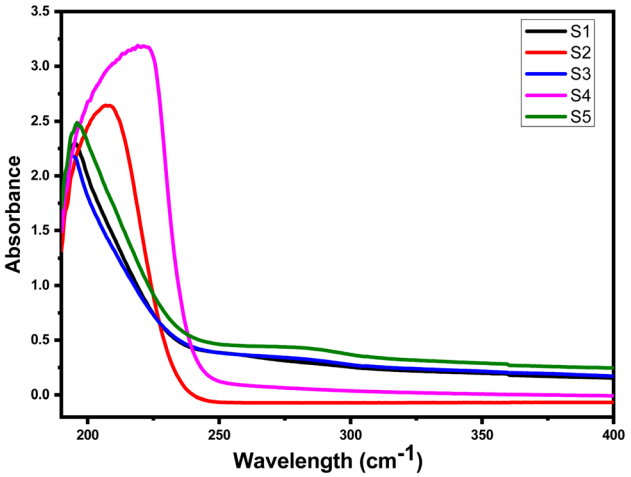

Fig. 4 UV-absorbance of HEC and HEC@$ZnCe_{0.3}Ti_{0.7}O_3$ nanocomposites.

microscopy (SEM). Fig. 3 presents SEM micrographs of HEC at two scan ranges (400× and 1000×) for HEC merged with 0 and 3 wt% $ZnCe_{0.3}Ti_{0.7}O_3$ nanocomposites. Micrographs (a and c) ascribed to the pure HEC and HEC loaded with 3 wt% $ZnCe_{0.3}Ti_{0.7}O_3$ at lower magnification (400×), while micrographs (b, d) show the same samples detected at higher magnification (1000×) for thorough surface analysis. The pure HEC micrographs (0%) reveal a relatively smooth, homogeneous surface morphology, suggesting a dense polymer network without visible nanoparticle dispersion.

Upon the merger of $ZnCe_{0.3}Ti_{0.7}O_3$ nanoparticles, as in Fig. 3c and d, prominent changes in surface texture are noted. At the doping level (3 wt%), the nanocomposite membrane surfaces show uniformly dispersed fine $ZnCe_{0.3}Ti_{0.7}O_3$ nanoparticles embedded within the polymer matrix, without noteworthy accumulation. The SEM micrographs show a branched texture in some areas of the surface, compared to the pristine HEC, indicating successful interaction among the HEC chains and with the $ZnCe_{0.3}Ti_{0.7}O_3$ nano-fillers. At the highest loading (3 wt%), the SEM micrographs (Fig. 3c and d) reveal more prominent surface smoothing and increased nanoparticle dispersion. This may be because of the combination of nanoparticles within the polymeric matrix. The elemental composition of HEC@$ZnCe_{0.3}Ti_{0.7}O_3$ nanocomposites was determined through EDX analysis (Fig. 3e). The EDX analysis confirms the atomic ratios of Ti (13.01%), Zn (10.33%), Ce (6.98%), C (22.62%), and O (46.97%).

The TEM image of the synthesized $ZnCe_{0.3}Ti_{0.7}O_3$ nanoparticles reveals a uniform nanoscale morphology (Fig. 3f), where most particles exhibit nearly spherical with hexagonal to slightly irregular geometries. The particles show a narrow size distribution (Fig. 3g), with an average diameter in the range of ≈6 to 16 nm, according to particle size histogram. Such a size range implies a high specific surface area and a large density of surface and near-surface active sites, which can enhance the surface-controlled processes. The nanoparticles appear well separated with clearly defined boundaries, indicating

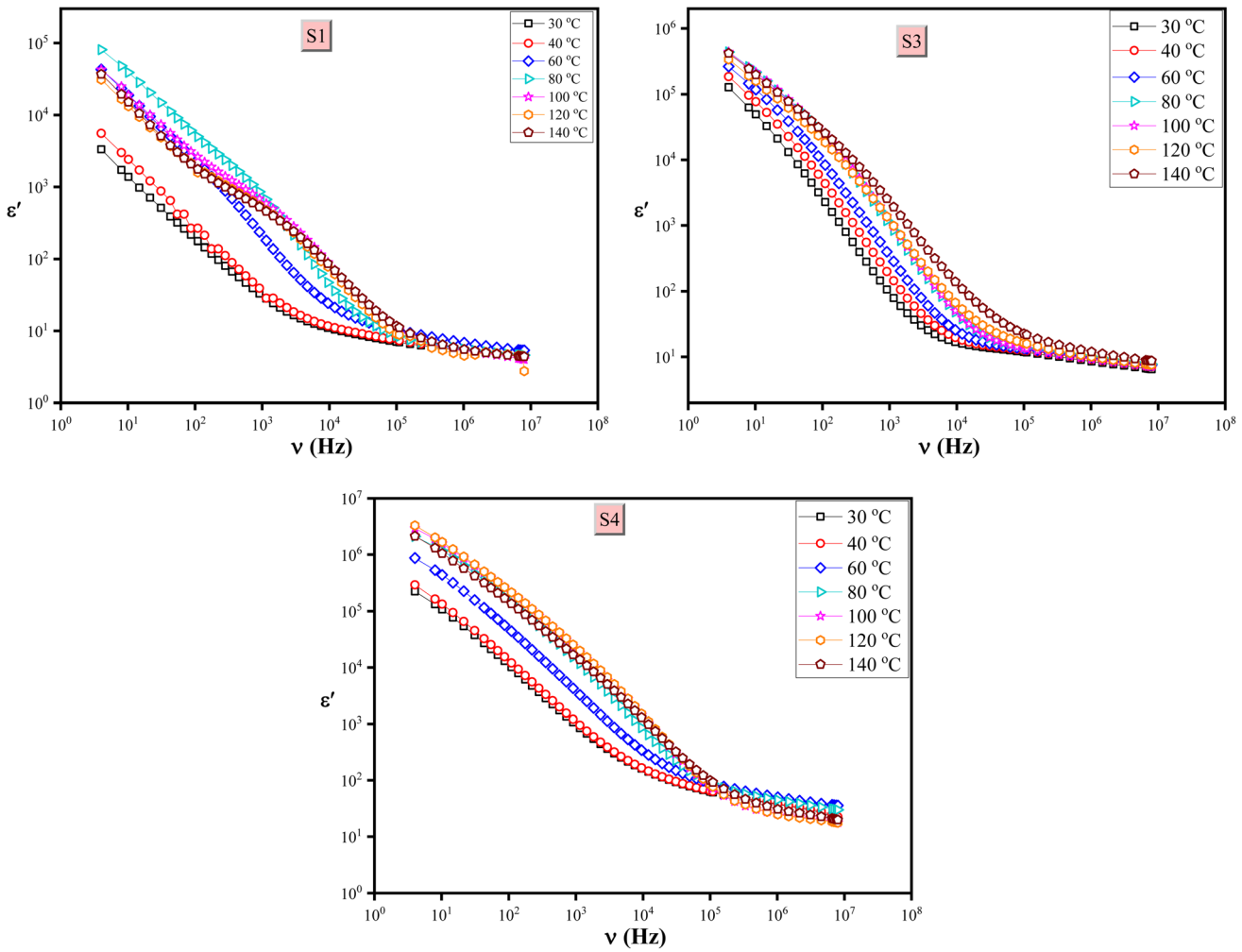

Fig. 5 Dielectric constant (ε') of HEC and HEC@ $ZnCe_{0.3}Ti_{0.7}O_3$ nanocomposites (S1, S3, and S4) at different temperatures (30 °C to 140 °C).

successful control over nucleation and growth during the sol–gel synthesis.

UV-absorbance

The UV-vis absorbance spectra of HEC incorporated with different weights of $ZnCe_{0.3}Ti_{0.7}O_3$ nanoparticles revealed a notable enhancement in optical absorption, particularly in the UV region (Fig. 4). This behavior can be attributed to the intrinsic electronic transitions within the $ZnCe_{0.3}Ti_{0.7}O_3$ spinel structure, which includes charge transfer transitions between O^{2-} and Ti^{4+}/Ce^{4+} ions. As the filler content increased, a systematic rise in absorbance intensity was observed, confirming the effective incorporation and light-interacting nature of the nanofillers within the HEC matrix. The most pronounced absorption enhancement was recorded at 3–4 wt%, indicating optimal nanoparticle dispersion and interaction with the polymer chains. Furthermore, a noticeable blue shift or stabilization of the absorption edge with increasing nanoparticle content may suggest a quantum confinement effect or improved interfacial interaction between the HEC and $ZnCe_{0.3}Ti_{0.7}O_4$ particles. This shift indicates bandgap modulation, suggesting that optical properties can be tuned with nanoparticle loading. The increased UV absorption also implies enhanced UV shielding, making these nanocomposite films promising candidates for UV-protective coatings, active packaging, and optoelectronic materials. Additionally, the strong light-harvesting capability could support potential photocatalytic or antimicrobial applications under UV exposure.

Dielectric properties

Fig. 5 provides the dielectric constant (ε') performance against frequency for HEC-based nanocomposites containing varying weights of $ZnCe_{0.3}Ti_{0.7}O_3$ (denoted as S1, S3, and S4) measured at different temperatures (30 °C to 140 °C). At lower frequencies, the dielectric constant (ε') is higher, indicating significant polarization effects, such as interfacial polarization and electrode polarization. As the frequency increases, the numerical value of the dielectric constant ε' decreases, which is typical for dielectric materials due to the inability of dipolar and interfacial polarizations to follow the rapidly oscillating electric field.[32–36]

The HEC matrix behaves as a flexible and insulating substrate. Its intrinsic polarization is lower than that of the

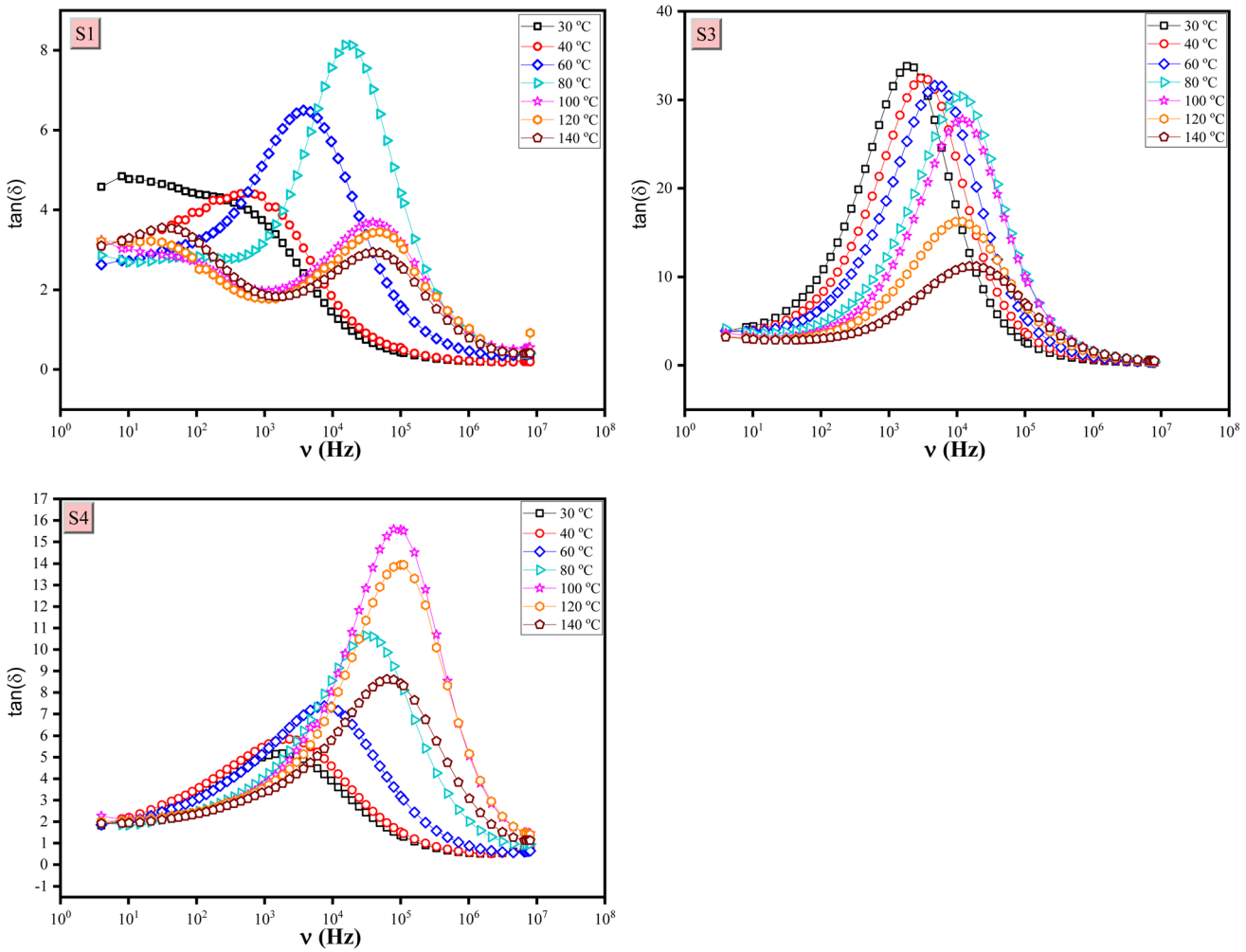

Fig. 6 Loss tangent (tan(δ)) of HEC and HEC@$ZnCe_{0.3}Ti_{0.7}O_3$ nanocomposites (S1, S3, and S4) at different temperatures (30 to 140 °C).

nanofiller $ZnCe_{0.3}Ti_{0.7}O_3$, but it facilitates uniform filler dispersion and enhances the composite's flexibility. Fig. 6 gives a clear presentation of the effect of the nanofiller $ZnCe_{0.3}Ti_{0.7}O_3$ on the dielectric constant trend. The HEC without $ZnCe_{0.3}Ti_{0.7}O_3$ (S1) displays a relatively moderate dielectric constant, while samples filled with nanofiller $ZnCe_{0.3}Ti_{0.7}O_3$ display enhanced dielectric constants compared to S1, suggesting that increasing $ZnCe_{0.3}Ti_{0.7}O_3$ concentration improves the dielectric properties. That trend can be attributed to $ZnCe_{0.3}Ti_{0.7}O_3$, which has a perovskite structure with a high dielectric constant; increasing its concentration improves the composite's overall dielectric constant by contributing intense dipolar polarization. At high concentrations, excessive $ZnCe_{0.3}Ti_{0.7}O_3$ can lead to agglomeration, reducing effective polarization and producing localized regions of dielectric heterogeneity, as observed in the S4 sample, where a pronounced reduction in the dielectric constant is observed at higher frequencies.[32,33,37–40] The effect of increasing temperature on the dielectric constant is observed in all samples, with the dielectric constant increasing at low frequencies. The increase in ε' with temperature can be attributed to the enhanced mobility of charge carriers and dipoles. This is consistent with the Debye relaxation behavior observed in polymer-based composites.[36,41–44] Also, the HEC matrix softens slightly at elevated temperatures, increasing the mobility of dipoles and charge carriers, thereby enhancing dielectric performance.

Fig. 6 illustrates the loss tangent (tan(δ)) of HEC@$ZnCe_{0.3}Ti_{0.7}O_3$ nanocomposites incorporating varying concentrations of $ZnCe_{0.3}Ti_{0.7}O_3$, denoted as S1, S3, and S4, across a temperature range of 30 to 140 °C and frequency range of 4 to 8 MHz. The loss tangent (tan(δ)) represents the energy dissipation in a material when subjected to an alternating electric field. Therefore, the loss tangent tan(δ) is an indicator of energy loss in materials, which can be crucial for electronics and materials science. The frequency dependence of tan(δ) shows distinct peaks at specific frequencies, as shown in Fig. 6. These peaks shift with temperature, indicating changes in the dielectric response of the material. Fig. 6 illustrates that as the temperature increases from 30 to 140 °C, the peak of tan(δ) shifts to higher frequencies. This shift can be attributed to the increased mobility of charge carriers, indicating thermally activated dipolar relaxation processes. At higher temperatures, thermal

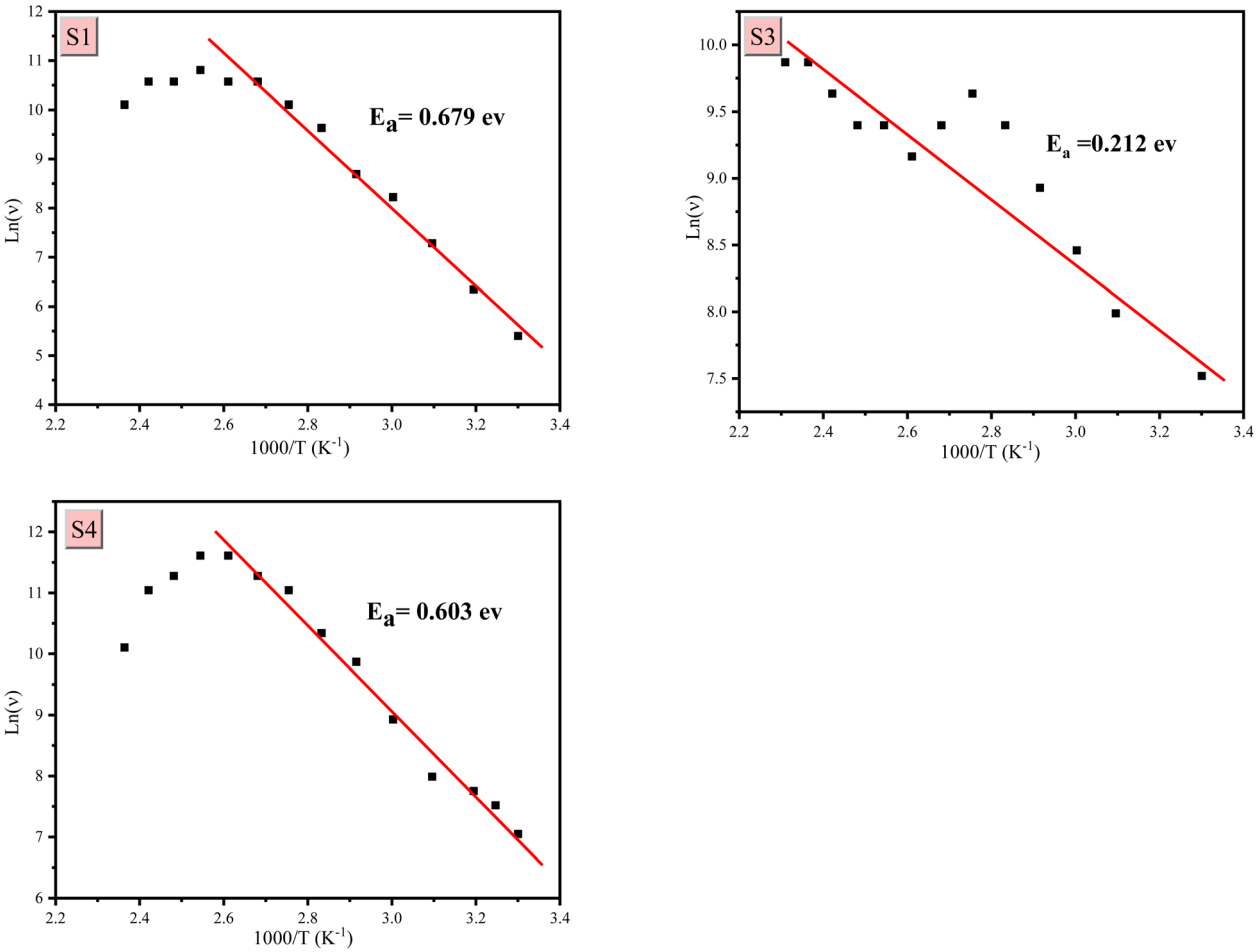

Fig. 7 Arrhenius plots of ln(ν) *versus* 1000/T for HEC and HEC@$ZnCe_{0.3}Ti_{0.7}O_3$ nanocomposites (S1, S3, and S4).

energy allows dipoles to reorient more rapidly, decreasing their relaxation time and shifting the peak to higher frequencies. S1 shows two loss peaks with higher frequencies at higher temperatures; the first peak at low frequency can be assigned to extrinsic effects, representing electrode and interfacial polarization, while the peak at high frequency corresponds to the intrinsic effect of segmental polarization in the HEC matrix.[33–35,37,38] Also, the relaxation peak's height and position were affected by the nanofiller concentration $ZnCe_{0.3}Ti_{0.7}O_3$, as depicted in Fig. 6. These findings emphasize the tunability of dielectric properties in HEC-based composites *via* adjustments in filler content and temperature, offering potential applications in advanced electronic and energy-storage devices.

Fig. 6 shows that S4 has the heist loss tangent peak at 100 °C, compared to those at elevated temperatures. The observed behavior can be assigned to the effect of residual moisture/solvent evaporation and interfacial Maxwell–Wagner–Sillars polarization.[45–48] At around 100 °C, the highest loss tangent can be attributed to the residual volatiles plasticizing the polymer matrix that resulting in an enhancement in the segmental mobility, allowing strong Maxwell–Wagner–Sillars interfacial polarization between the Hydroxyethyl cellulose phase and the ceramic clusters, thereby enhancing the relaxation peak.[46,49] With increasing temperature, the volatile component is likely driven off, and therefore reduces its plasticizing effect that leading to a decrease in the loss tangent peak height.

The reciprocal of the relaxation frequence define the relaxation time. The relation between the relaxation frequency and temperature can be used to estimate the activation energy through the Arrhenius relation as following:

$$\nu_{rel} = \nu_0 \exp\left(-\frac{E_a}{k_B T}\right)$$

where the Boltzmann constant is $k_B = 8.6173 \times 10^{-5}$ eV K^{-1} and E_a represents the activation energy that estimated from the slop of the ln(ν) *vs.* (1000/T) curve as presented in Fig. 7. The estimated activation energies were found to be 0.679 eV for S1, 0.212 eV for S3, and 0.603 eV for S4. The substantial decrease in activation energy at 1.0 wt% $ZnCe_{0.3}Ti_{0.7}O_3$ (S3) signifies a lower barrier for dipolar/ionic motion, indicating that the filler concentration creates more efficient conduction pathways within the Hydroxyethyl cellulose matrix. At higher loading (S4), the activation energy increases but less than the activation energy of the virgin polymer, suggesting partial blocking of pathways due to filler agglomeration.

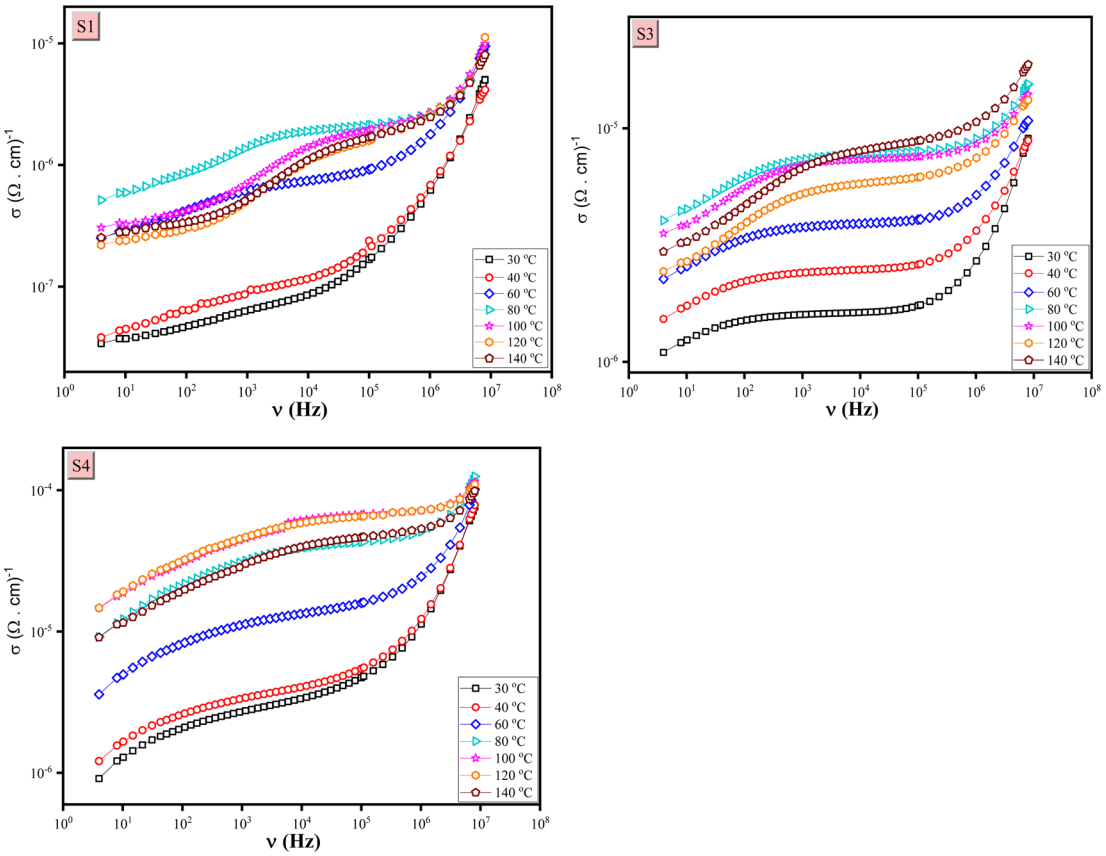

Fig. 8 AC conductivity (σ) of HEC and HEC@ $ZnCe_{0.3}Ti_{0.7}O_3$ nanocomposites (S1, S3, and S4) at different temperatures (30 to 140 °C).

AC conductivity

The data provided in Fig. 8 shows the ac conductivity (σ_{ac}) of HEC@$ZnCe_{0.3}Ti_{0.7}O_3$ nanocomposites across a temperature range (30–120 °C) as a function of frequency (ν). The observed trend shows a slow increase in conductivity at low frequencies and a rapid increase at high frequencies. The composites' frequency-dependent behavior indicates interfacial polarization (Maxwell–Wagner–Sillars effect) at low frequencies and ionic/electronic hopping at higher frequencies. This behavior is typical for heterogeneous systems where heterogeneous phases (inorganic/organic) interact to produce complex dielectric responses. The increasing conductivity with frequency at higher frequencies can be attributed to the hopping conduction mechanism, in which charge carriers gain sufficient energy to overcome potential barriers between wells. At the same time,

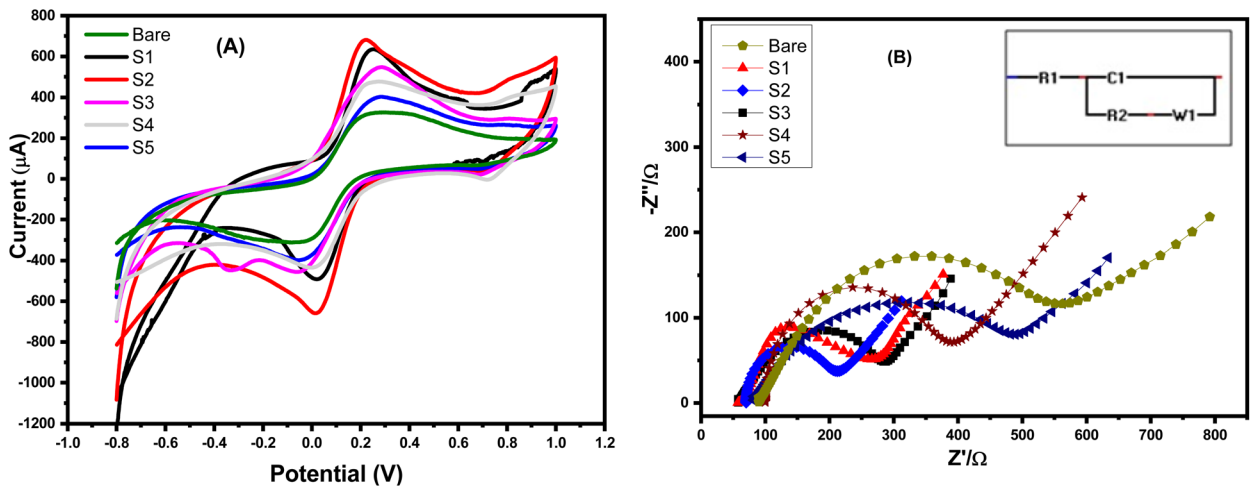

Fig. 9 (A) CV measurements (B) EIS Nyquist spectra of bare (unmodified SPE), S1, S2, S3, S4, and S5 modified SPEs were produced in a solution of ferri/ferrocyanide (5 mM) and 0.1 M KCl. (inserted in B) EIS data fitting circuit.

Table 1 CV & EIS electrochemical characterization data which obtained for HEC and HEC@$ZnCe_{0.3}Ti_{0.7}O_3$ nanocomposites modified SPEs. For EIS data obtained after fitting the data using the circuit which presented in Fig. 9b inset[a]

Electrode modified	I_a (μA)	I_c (μA)	$E_{oxd.}$ (V)	$E_{red.}$ (V)	$E_{1/2}$ (V)	R_s (Ω)	$R_{ct\ (1)}$ (Ω)	C (μF)	W (Ω)
Bare	331	−305	0.3	−0.007	0.1465	89.6	682	0.98	0.0005
S1	641	−498	0.25	0.021	0.1355	65.6	167.6	3.908	0.00189
S2	698	−655	0.217	0.007	0.112	70.07	125.1	4.28	0.00238
S3	558	−454	0.282	−0.04	0.121	95.17	260.4	1.53	0.00109
S4	471	−437	0.253	0.007	0.13	99.6	257.4	1.753	0.00118
S5	414	−401	0.279	−0.061	0.109	101.7	350	1.27	0.0009

[a] Anodic current (I_a), cathodic current (I_c), potential of oxidation (E_{oxd}), potential of reduction (E_{red}), solution resistance (R_s), charge transfer resistance (R_{ct}), constant phase element (CPE), Warburg resistance (W), and specific capacitance (C).

the low conductivity at low frequencies is attributed to the blocking of charge carriers at grain boundaries or interfaces. The observed frequency dependence of conductivity aligns with the Universal power law in disordered systems.[50] The observed behavior is characteristic of the composite material, in which the nanofiller $ZnCe_{0.3}Ti_{0.7}O_3$ and the polymer matrix (HEC) form a heterogeneous structure; therefore, the interplay between ionic conduction from the nanofiller and the insulating HEC matrix governs the overall conductivity.

Fig. 8 demonstrates the effect of heating energy on the conductivity of the HEC and HEC@$ZnCe_{0.3}Ti_{0.7}O_3$ nanocomposites through increasing the ambient temperature from 30 °C to 140 °C. According to Fig. 8, the conductivity increases with increasing temperature. This behavior indicates thermal activation of charge carriers, in which elevated thermal energy enables them to overcome localized energy barriers and enhances their mobility. This behavior aligns with the hopping conduction mechanism, in which higher thermal energy reduces the potential barrier to carrier movement, thereby enhancing conductivity.

Fig. 8 shows that S3 and S4 have higher conductivity than S1. The enhancement in conductivity can be attributed to the fact that $ZnCe_{0.3}Ti_{0.7}O_3$ nano fillers increase the density of mobile charge carriers and promote ionic conduction by increasing the conduction network pathways for charge transport.[50]

Electrochemical characterization

To evaluate the electrochemical behavior of the synthesized nanomaterials, the surfaces of screen-printed electrodes (SPEs) were modified *via* drop-casting with the nanocomposites, followed by cyclic voltammetry (CV) and electrochemical impedance spectroscopy (EIS) measurements. These tests were conducted using a mixed solution containing 0.1 M KCl and 5 mM $K_3[Fe(CN)_6]$. The CV results (Fig. 9A) showed significantly higher redox peak currents for all nanocomposite-modified electrodes compared to the unmodified (bare) SPE, indicating enhanced electrochemical activity. As illustrated in Fig. 9A, the oxidation and reduction peak currents increased in the order: bare < S5 < S4 < S3 < S1 < S2. The oxidation peak currents recorded were 331, 414, 471, 558, 641, and 698 μA, respectively. The S2-modified electrode exhibited the highest redox current, demonstrating superior electrocatalytic performance. Similarly, EIS analysis (Fig. 9B) using the fitted circuit which presented into Fig. 9B (which containing R_1: resistance of solution, R_2: charge transfer resistance, W_1: Warburg resistance and C: capacitance) confirmed the improved charge transfer properties of the nanocomposites. The S2-modified electrode displayed the lowest charge transfer resistance ($R_{ct} = 125\ \Omega$), compared with the bare electrode ($R_{ct} = 682\ \Omega$). The R_{ct} values for the S1, S3, S4 and S5 modified electrodes were 167, 260, 257, and 350 Ω, respectively. These results confirm enhanced electron-transfer efficiency at the S2 electrode interface. A summary of the electrochemical performance data for all modified SPEs is provided in Table 1.

Electrochemical surface area and capacitance evaluation

To further assess the electrochemically active surface area (EASA) of screen-printed electrodes (SPEs) modified with the synthesized S1, S2, S3, S4, and S5 samples, as well as the unmodified SPE voltammetric experiments were conducted in a 0.1 M KCl solution containing 5 mM ferro/ferri cyanide. As illustrated in Fig. 10, all electrodes displayed a linear increase in redox peak current with increasing scan rate, indicating diffusion-controlled electrochemical behavior. Notably, the SPE modified with S2 showed the most prominent linear redox response (Fig. 11), suggesting superior electrochemical kinetics. The EASA was estimated using the Randles–Ševčík equation:[34]

$$I_p = 2.69 \times 10^5 \times n^{3/2} \times A \times D^{1/2} \times C \times \nu^{1/2}$$

where I_p is the peak current (A), n is the number of electrons transferred, D is the diffusion coefficient ($cm^2\ s^{-1}$), A is the electrochemically active surface area (cm^2), C is the concentration of FCN (mol L^{-1}), and ν is the scan rate (V s^{-1}).

Anodic (I_{pa}) and cathodic (I_{pc}) peak currents were plotted against the square root of the scan rate (figure insets), revealing a strong linear relationship with a correlation coefficient of 0.991. Based on these data, the calculated EASA values for unmodified, S1, S2, S3, S4, and S5 SPEs are 0.087, 0.1245, 0.204, 0.0855, 0.0581, and 0.0482 cm^2.

This substantial enhancement in surface area, particularly for the S2-modified electrode, confirms its superior electrochemical activity. Additionally, the specific capacitance (C) of each electrode was determined using the equation:

$$C = \left(\int I\,dV\right) \Big/ (2 \times \nu \times m \times \Delta V)$$

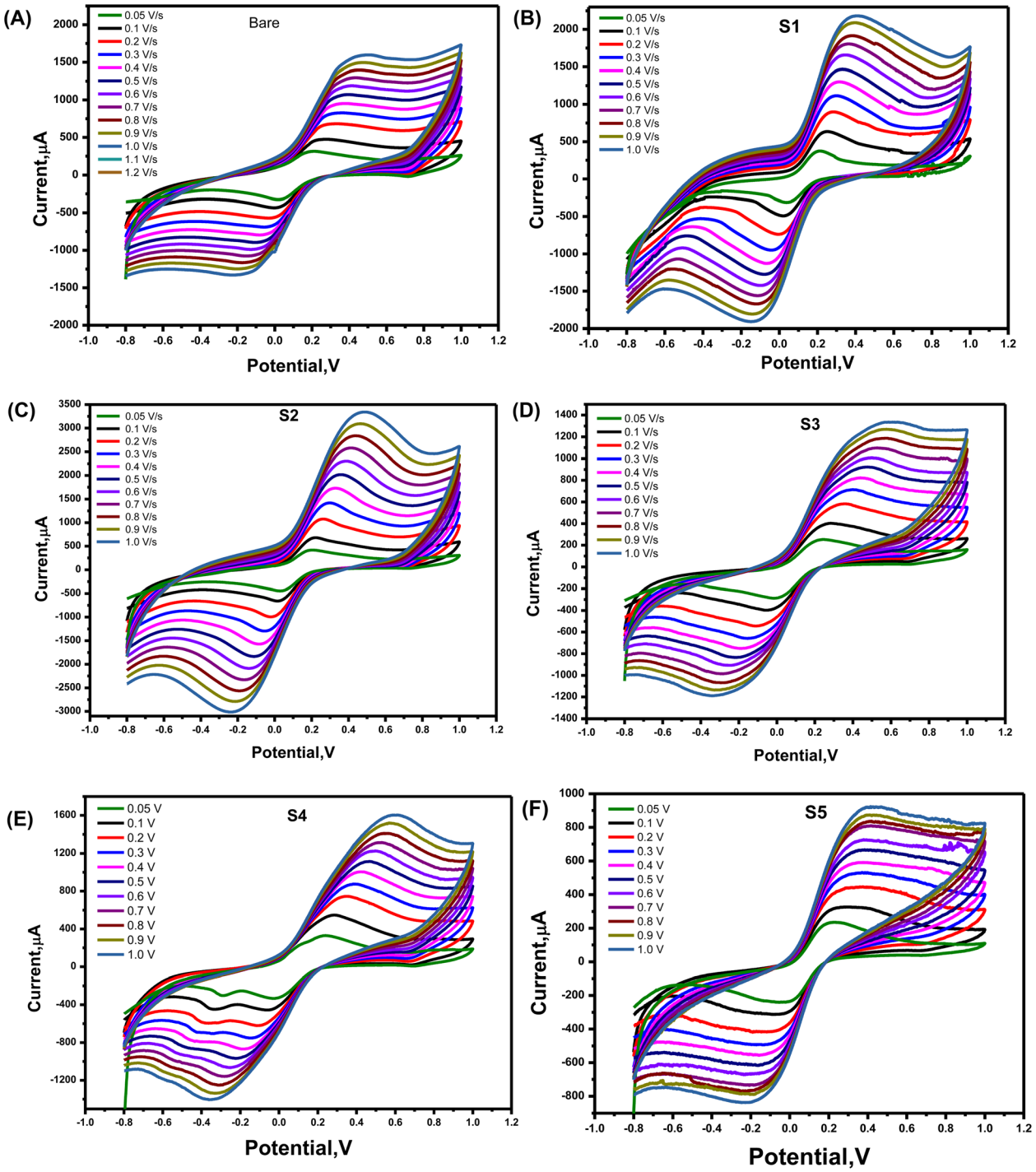

Fig. 10 Cyclic voltammograms of (A) Bare, (B) S1, (C) S2, (D) S3 (E) S4, and (F) S5 modified screen printed electrodes at different scan rates from 50–1000 mV s^{-1} in a solution containing 5 mM ferro/ferri cyanide and 0.1 M KCl.

where C is the specific capacitance (F g^{-1}), $\int IdV$ is the area under the CV curve, ΔV is the potential window (V), m is the mass of active material (g), and ν is the scan rate (V s^{-1}).

All electrodes exhibited excellent electrochemical stability across varying scan rates, with no observable degradation or structural damage. Significant improvements in capacitance were observed upon modification with the nanocomposites. Among them, the S2-modified SPE demonstrated the highest capacitance across all scan rates. At a scan rate of 50 mV s^{-1}, the specific capacitance values of unmodified SPE, S1, S2, S3, S4, and S5-modified SPE are 812, 1050, 1210, 872, 1065, and 624 F g^{-1}. These findings clearly establish the enhanced electrochemical performance of the S2 nanocomposite-modified electrode. Supporting data are presented in Fig. 12.

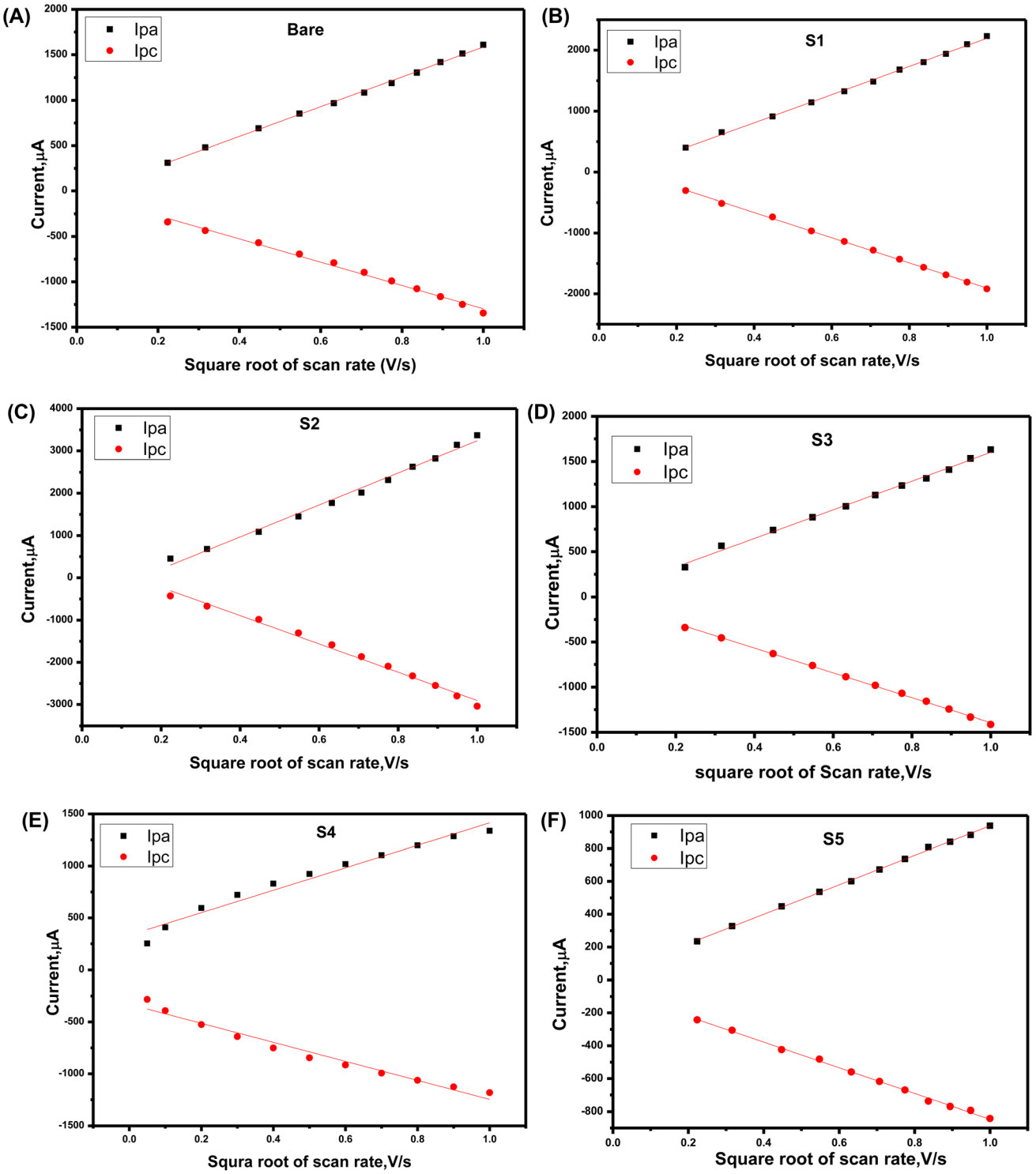

Fig. 11 Anodic (I_{pa}) and cathodic (I_{pc}) peak currents *vs.* the square root of the scan rate of (A) bare, (B) S1 (C) S2, (D) S3 (E) S4, and (F) S5 modified screen printed electrodes using a solution containing 5 mM ferro/ferri cyanide and 0.1 M KCl.

Electrochemical sensing application of S2 modified SPE for H_2O_2 detection

The primary goal of this study was to explore novel nanomaterials with enhanced electrochemical properties and efficient electron transfer capabilities for application in sensor technologies. To this end, various synthesized nanocomposites were evaluated as surface modifiers on screen-printed electrodes (SPEs) for the development of a non-enzymatic hydrogen peroxide (H_2O_2) sensor.

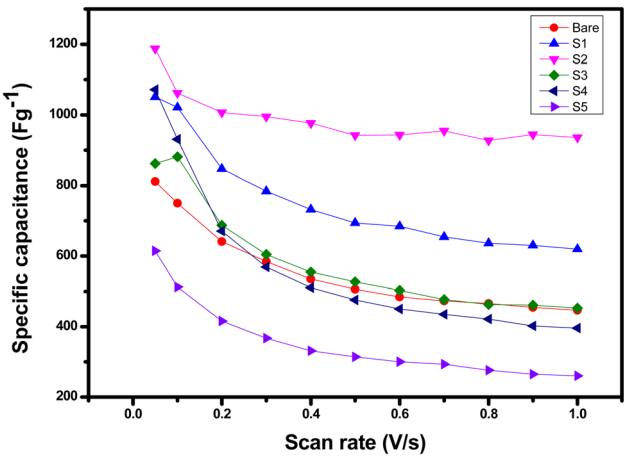

Fig. 12 Linearity curve between specific capacitance values *vs.* scan rate of unmodified bare and modified screen-printed electrodes with HEC and HEC@$ZnCe_{0.3}Ti_{0.7}O_3$ nanocomposites.

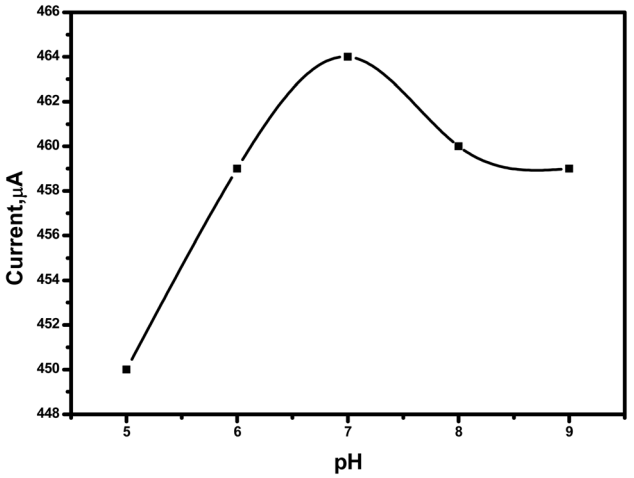

Fig. 13 pH effect of PBS buffer on the chronoamperometry peaks current of peroxide oxidation using the HEC and HEC@$ZnCe_{0.3}Ti_{0.7}O_3$ nanocomposites modified SPEs.

Effect of pH

To further optimize the sensor performance, the influence of phosphate buffer solution (PBS) pH on the oxidation peak current of hydrogen peroxide was investigated using the S2-modified SPE. Measurements were conducted using the chronoamperometry (CA) technique.

As shown in Fig. 13, the oxidation current increased progressively with rising pH, reaching a maximum at pH 7.0. Beyond this point, a decline in peak current was observed. Based on these results, PBS with pH 7.0 was identified as the optimal medium and was selected for all subsequent experiments.

Peroxide detection

The sensor's performance was evaluated using chronoamperometry (CA). In these experiments, varying concentrations of H_2O_2 were added to a phosphate buffer solution (pH ~ 7), and the electrochemical response was recorded.

Among the tested materials, the S2 nanocomposite-modified SPE demonstrated the highest electrocatalytic efficiency for the direct oxidation of H_2O_2. The structural features of the nanocomposite significantly contributed to its excellent catalytic performance, enabling sensitive and reliable detection of H_2O_2.

Chronoamperometric measurements (Fig. 14A and B) further validated the excellent performance of the sensor. It exhibited a high sensitivity of 0.998 μA μM^{-1} and a broad linear detection range spanning from 0.05 to 2000 μM. The strong linearity was confirmed by an R^2 value of 0.997. Notably, the sensor achieved a low limit of detection (LOD) of 0.02 μM and a limit of quantification (LOQ) of 0.04 μM.

These findings highlight the superior electrocatalytic activity and outstanding sensing capabilities of the S2-modified screen-printed electrode (SPE) for hydrogen peroxide detection. A comparative analysis with previously reported H_2O_2 sensors (Table 2) reveals that the S2-based sensor surpasses many existing systems in terms of sensitivity, detection range, and

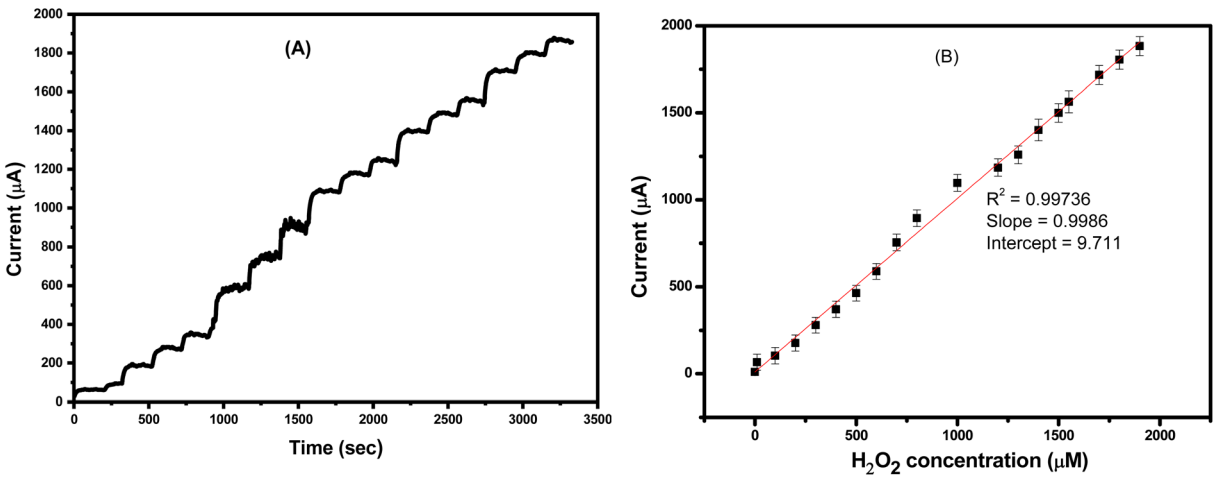

Fig. 14 (A) Chronoamperometric (CA) responses recorded at a fixed potential of 0.7 V, and (B) the corresponding linear calibration curve of current *versus* H_2O_2 concentration with $R^2 = 0.997$. The measurements were performed using the S2 electrode after successive additions of various H_2O_2 concentrations in PBS buffer (pH 7.0).

Table 2 Comparison between different H_2O_2 sensors[a]

Electrode	Linear range (μM)	Detection limit (μM)	Applied potential	Ref.
$MnCo_2O_3$/CNTs	0.1–180	0.1	0.7	51
Pt/rGO-CNT	0.1–25	0.1	−0.25	52
Co_3O_4/SPE	0.1–50	0.145	1.0	53
rGo-Pt	0.5–3475	0.2	−0.08	54
Pol(azureA)-PtNPs	0–300	0.052	0.1	55
Co_3O_4_rGO	15–675	2.4	−0.19	56
$NiCo_2O_4$/rGO	5–3000	0.41	−0.4	57
poly(MMA/DMAEMA/CHAA)/TiO_2	1 to 800 μM	—	0.7	58
poly(MMA/DMAEMA/AA)/MnO_2	1–1000 μM	0.03 μM	0.7	59
$ZnCe_{0.3}Ti_{0.7}O_3$	0.05–2000	0.02	0.7	This work

[a] rGO: reduced graphene oxide PtNPs: platinum nanoparticles CNTs: carbon nanotube.

LOD. This underscores the strong potential of the S2 nanocomposite as an efficient material for non-enzymatic hydrogen peroxide sensing applications.

Mechanism of H_2O_2 detection using $ZnCe_{0.3}Ti_{0.7}O_3$/HEC-modified non-enzymatic sensor

The $ZnCe_{0.3}Ti_{0.7}O_3$/HEC-modified electrode detects hydrogen peroxide through a cooperative mechanism involving the matrix. The $ZnCe_{0.3}Ti_{0.7}O_3$ nanostructures supply numerous redox-active sites—primarily Ce^{3+}/Ce^{4+} and Ti^{3+}/Ti^{4+} pairs—that enable rapid electron exchange and accelerate the catalytic decomposition of H_2O_2. As hydrogen peroxide reaches the electrode, it permeates the hydrated, porous HEC network and adsorbs onto the nanoparticle surfaces, where it undergoes potential-dependent oxidation or reduction. The reversible transitions between $Ce^{3+} \leftrightarrow Ce^{4+}$ and $Ti^{3+} \leftrightarrow Ti^{4+}$ act as efficient electron mediators, lowering the energy barrier for H_2O_2 dissociation and generating a distinct faradaic response. The HEC scaffold not only stabilizes the dispersion of nanoparticles but also enhances ion mobility and electron transport at the interface, ensuring faster access of H_2O_2 to catalytic sites. Together, these features endow the $ZnCe_{0.3}Ti_{0.7}O_3$/HEC composite with outstanding electrocatalytic performance, rapid charge-transfer kinetics, and strong affinity toward hydrogen peroxide, leading to highly sensitive and selective non-enzymatic sensing even in complex sample environments.

Schematic diagram for peroxide detection mechanism

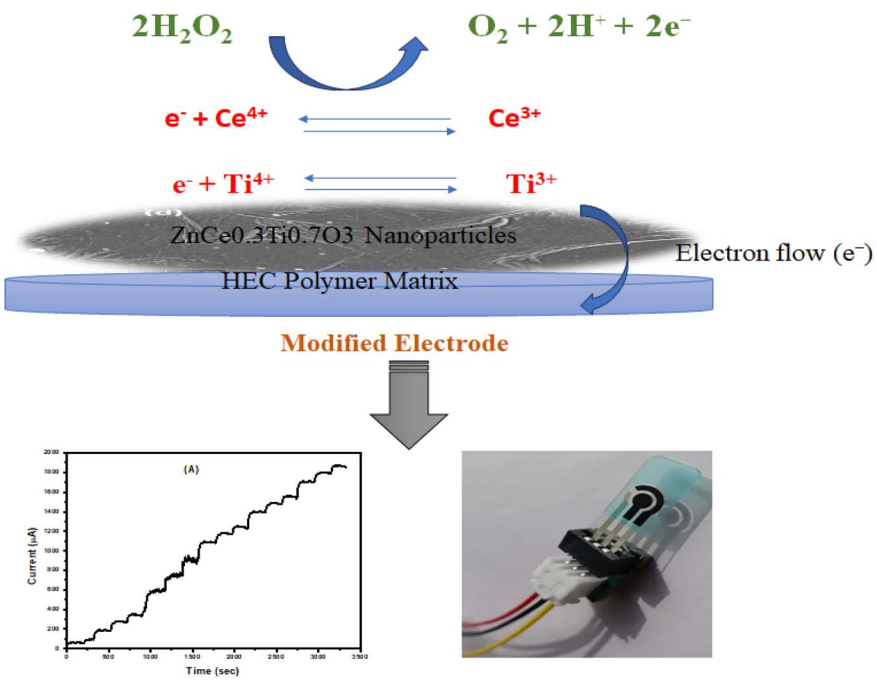

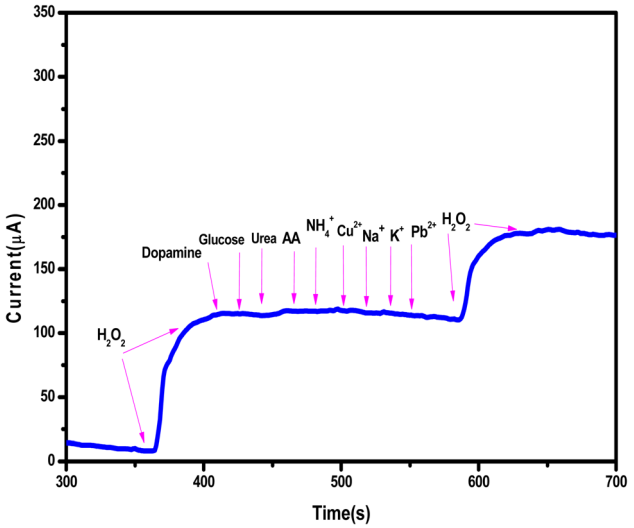

Fig. 15 Chronoamperometric responses of the 100 μM peroxide (targeting analyte), and 0.1 M of non-targeting analytes in phosphate buffer pH (7.0) at a fixed potential of 0.7 V.

Selectivity evaluation of the hydrogen peroxide sensor

Because the sensor is designed for application in real-world samples, it is expected to encounter complex matrices that contain numerous electroactive species. For this reason, examining its selectivity toward hydrogen peroxide in the presence of common interfering compounds is essential. To assess this, individual 0.1 M solutions of typical interferents—such as sodium nitrate ($NaNO_3$), potassium chloride (KCl), lead nitrate ($Pb(NO_3)_2$), copper nitrate ($Cu(NO_3)_2$), ascorbic acid (AA), urea, glucose, and dopamine—were prepared. Their potential impact on the sensor's performance was examined using amperometric (CA) measurements in comparison with the response toward 100 μM H_2O_2.

The results demonstrated that these species produced negligible current responses, indicating no significant interference at the electrode surface. In contrast, successive additions of hydrogen peroxide generated an immediate and pronounced rise in current, even when mixtures of the tested interferents were present (Fig. 15).

Overall, the outcomes confirm that the fabricated sensor possesses outstanding selectivity, high sensitivity, and rapid response characteristics, making it highly suitable for accurate peroxide detection within complex sample environments.

Conclusion

The successful loading of $ZnCe_{0.3}Ti_{0.7}O_4$ NPs into the HEC matrix, proved by the absence of voids or cracks, designates durable interfacial compatibility between the nanofillers and the polymer. This well-bonded interface confirms the structural strength of the nanocomposite.

The SEM reveals that the addition of $ZnCe_{0.3}Ti_{0.7}O_4$ nanoparticles remarkably alters the surface topography of the HEC films. The EDX confirms the presence of $ZnCe_{0.3}Ti_{0.7}O_4$ nanoparticles and supports that their addition significantly modifies the surface morphology of the HEC composites. These changes offer promising improvements in the material's barrier performance, electrochemical behavior, electrical properties, and potential bioactivity, making the nanocomposite a promising candidate for advanced multifunctional applications.

The studied dielectric properties indicate that the addition of $ZnCe_{0.3}Ti_{0.7}O_3$ improves the dielectric and conductivity properties of HEC-based nanocomposites. The tunable dielectric constant, loss tangent, and conductivity as a function of filler concentration and temperature make these composites promising materials for electrochemical sensor applications. The nanocomposite was used to modify a screen-printed electrode surface for a non-enzymatic sensor for peroxide detection, with high sensitivity and selectivity, a linear range of 0.05–2000 μM, and a lower detection limit of 0.02 μM.

The integration of $ZnCe_{0.3}Ti_{0.7}O_4$ NPs improved the dielectric, electrochemical, and structural stability of the HEC-based nanocomposites, making them promising candidates for multifunctional applications such as UV-protective coatings, energy storage, supercapacitors, bioactive films, and environmentally friendly optoelectronic devices.

Conflicts of interest

The authors report no conflict of interest. The authors alone are responsible for the content and writing of the paper.

Data availability

The data that support the findings of this study are available from the corresponding author upon reasonable request.

References

1 A. M. Abouelnaga and A. M. El Nahrawy, Spectroscopic investigation, dielectric and antimicrobial properties of chitin-cellulose@ZnO/CuO conductive nanocomposites, *Spectrochim. Acta, Part A*, 2024, **320**, 124646.
2 A. B. Abou Hammad and A. M. El Nahrawy, Spinel Sensors and Biosensors, *Handbook of Nanosensors*, 2024, pp. 427–459, DOI: 10.1007/978-3-031-47180-3_34/FIGURES/11.
3 H. S. Magar, A. M. El Nahrawy and A. B. Abou Hammad, Progressing Energy Storage and Antimicrobial Nanochitosan-Li_2CaO_2@Flumox Nanocomposites, *Polym. Adv. Technol.*, 2025, **36**, e70191.
4 S. Kamel and N. S. El-Sayed, Cellulose and its Derivatives: Towards Green Inhibitors of Metal Corrosion, *Egypt. J. Chem.*, 2023, **66**, 2119–2139.
5 A. M. E. Nahrawy, A. A. Haroun, A. B. A. Hammad, M. A. Diab and S. Kamel, Uniformly Embedded Cellulose/Polypyrrole-TiO_2 Composite in Sol–Gel Sodium Silicate Nanoparticles: Structural and Dielectric Properties, *Silicon*, 2019, **11**, 1063–1070.
6 A. M. El, A. M. Mansour, A. Elzwawy, A. B. Abou and B. A. Hemdan, Environmental Nanotechnology , Monitoring & Management Spectroscopic and magnetic

properties of pathogenic bacteria during sewage handling, *Environ. Nanotechnol., Monit. Manage.*, 2022, **18**, 100672.

7 A. B. Abou Hammad, A. A. Al-esnawy, A. M. Mansour and A. M. El Nahrawy, Synthesis and characterization of chitosan-corn starch-SiO_2/silver eco-nanocomposites: exploring optoelectronic and antibacterial potential, *Int. J. Biol. Macromol.*, 2023, **249**, 126077.

8 Q. Wang, L. Zhong, Y. Zhou, G. Huang, J. Liu, H. Liu and Q. Zhu, Hierarchical cellulose nanopaper origami electronics, *Carbohydr. Polym.*, 2026, **373**, 124627.

9 M. Sheraz, *et al.*, Cellulose-Based Electrochemical Sensors, *Sensors*, 2025, **25**, 645.

10 X. Sun, *et al.*, Enhanced Antimicrobial Cellulose/Chitosan/ZnO Biodegradable Composite Membrane, *Membranes*, 2022, **12**, 239.

11 N. S. El-Sayed, H. Awad, G. M. El-Sayed, Z. A. Nagieb and S. Kamel, Synthesis and characterization of biocompatible hydrogel based on hydroxyethyl cellulose-g-poly(hydroxyethyl methacrylate), *Polym. Bull.*, 2020, **77**, 6333–6347.

12 J. Chen, D. Wang and J. Fu, Stiff yet Tough, Moisture-Tolerant, Room Temperature Self-Healing and Thermoconductive Biomimetic Nanocomposites, *Adv. Mater.*, 2025, **37**(42), e7548.

13 F. Zia, *et al.*, Preparation of hydroxyethyl cellulose/halloysite nanotubes graft polylactic acid-based polyurethane bionanocomposites, *Int. J. Biol. Macromol.*, 2020, **153**, 591–599.

14 J. U. Michaelis, S. Kiese, S. Hofmann, T. Lohner and P. Eisner, Elastohydrodynamic lubrication of aqueous hydroxyethyl cellulose-glycerol lubricants, *Tribol. Int.*, 2025, **206**, 110563.

15 M. Zhao, *et al.*, Exploration of hydroxyethyl cellulose-templated PEDOT:PSS for the development of high-performance conductive dual-network hydrogel strain sensor, *Chem. Eng. J.*, 2025, **519**, 165000.

16 T. Nongnual, N. Butprom, S. Boonsang and S. Kaewpirom, Citric acid crosslinked carboxymethyl cellulose edible films: a case study on preserving freshness in bananas, *Int. J. Biol. Macromol.*, 2024, **267**, 131135.

17 J. Sotolářová, Š. Vinter and J. Filip, Cellulose derivatives crosslinked by citric acid on electrode surface as a heavy metal absorption/sensing matrix, *Colloids Surf., A*, 2021, **628**, 127242.

18 B. R. Estevam, I. D. Perez, Â. M. Moraes and L. V. Fregolente, A review of the strategies used to produce different networks in cellulose-based hydrogels, *Mater. Today Chem.*, 2023, **34**, 101803.

19 A. M. Mansour, H. S. Magar, A. Elzwawy, A. B. Abou Hammad and A. M. El Nahrawy, Structural, optical, and electrochemical properties of tungsten-doped cadmium zinc phosphate nanoporous materials for energy storage and peroxide detection, *RSC Adv.*, 2025, **15**, 15670–15693.

20 A. Elzwawy, *et al.*, Exploring the structural and electrochemical sensing of wide bandgap calcium phosphate/$Cu_xFe_{3-x}O_4$ core-shell nanoceramics for H_2O_2 detection, *Mater. Today Commun.*, 2022, **33**, 104574.

21 H.-A. S. Tohamy and H. S. Magar, A Flexible, Low-Cost, Disposable Non-Enzymatic Electrochemical Sensor Based on MnO_2/Cellulose Nanostructure, *ECS J. Solid State Sci. Technol.*, 2022, DOI: 10.1149/2162-8777/acad27.

22 M. Y. Ali, H. B. Abdulrahman, W. T. Ting and M. M. R. Howlader, Green synthesized gold nanoparticles and CuO-based nonenzymatic sensor for saliva glucose monitoring, *RSC Adv.*, 2024, **14**, 577–588.

23 E. Ouda, N. Yousf, H. S. Magar, R. Y. A. Hassan and E. S. M. Duraia, Electrochemical properties of MnO_2-based carbon nanomaterials for energy storage and electrochemical sensing, *J. Mater. Sci.: Mater. Electron.*, 2023, **34**, 1–14.

24 H. S. Magar, M. S. Hashem and R. A. Sobh, Design of metal oxide nanoparticles-embedded polymeric nanocomposites for hydrogen peroxide chronoamperometric sensor, *Polym. Compos.*, 2023, DOI: 10.1002/PC.28017.

25 H. S. Magar, A. M. El Nahrawy, R. Y. A. Hassan and A. B. Abou Hammad, Nanohexagonal iron barium titanate nanoparticles surface-modified $NiFe_2O_4$ composite screen-printed electrode for enzymatic glucose monitoring, *RSC Adv.*, 2024, **14**, 34948–34963.

26 F. Zia, *et al.*, Synthesis and characterization of hydroxyethyl cellulose copolymer modified polyurethane bionanocomposites, *Int. J. Biol. Macromol.*, 2021, **179**, 345–352.

27 A. abou hammad, Development of dielectric and magnetic properties of advanced nano-engineering composites, *Egypt. J. Chem.*, 2022, **65**, 141–154.

28 A. M. El-Nahrawy, A. B. Abou Hammad, T. A. Khattab, A. Haroun and S. Kamel, Development of electrically conductive nanocomposites from cellulose nanowhiskers, polypyrrole and silver nanoparticles assisted with Nickel(III) oxide nanoparticles, *React. Funct. Polym.*, 2020, **149**, 104533.

29 A. M. El Nahrawy, *et al.*, Talented $Bi_{0.5}Na_{0.25}K_{0.25}TiO_3$/oxidized cellulose films for optoelectronic and bioburden of pathogenic microbes, *Carbohydr. Polym.*, 2022, **291**, 119656.

30 A. A. Haroun, *et al.*, Polyacetal/graphene/polypyrrole and cobalt nanoparticles electroconducting composites, *Int. J. Ind. Chem.*, 2020, **11**, 223–234.

31 A. B. Abou Hammad, H. S. Magar, F. Cao, T. Y. M. El-Ashkar and A. M. El Nahrawy, Structural, dielectric, and electrochemical properties of pear-shaped $Ce_xLi_2Zn_{0.5}Mn_{0.5}Ti_{3-x}O_8$ supercapacitor: XRD and dielectric calculation, *Phys. Scr.*, 2023, **98**, 125985.

32 A. M. El Nahrawy, A. M. Bakr, B. A. Hemdan and A. B. Abou Hammad, Identification of Fe^{3+} co-doped zinc titanate mesostructures using dielectric and antimicrobial activities, *Int. J. Environ. Sci. Technol.*, 2020, **17**, 4481–4494.

33 S. Dacrory, A. B. Abou Hammad, A. M. El Nahrawy, H. Abou-Yousef and S. Kamel, Cyanoethyl Cellulose/$BaTiO_3$/GO Flexible Films with Electroconductive Properties, *ECS J. Solid State Sci. Technol.*, 2021, **10**, 083004.

34 G. Qu, H. Cui, Y. Zhu, L. Yang and S. Li, Substantial Improvement of the Dielectric Strength of Cellulose–Liquid

Composites: Effects of Traps at the Nanoscale Interface, *J. Phys. Chem. Lett.*, 2020, **11**, 1881–1889.

35 Y. Shen, *et al.*, Enhanced energy density in cellulose doped polyimide-based all organic composites for high temperature capacitor applications, *J. Phys. D Appl. Phys.*, 2024, **57**, 375501.

36 J. Jose, *et al.*, Effect of temperature and frequency on the dielectric properties of cellulose nanofibers from cotton, *J. Mater. Sci.: Mater. Electron.*, 2021, **32**, 21213–21224.

37 S. C. Shi, *et al.*, Environmentally friendly regenerated cellulose films with improved dielectric properties *via* manipulating the hydrogen bonding network, *Appl. Phys. Lett.*, 2021, **119**(2), 022903.

38 M. Lecoublet, M. Ragoubi, N. Leblanc and A. Koubaa, Optimizing the Dielectric and Mechanical Performance of 3D-Printed Cellulose-Based Biocomposites and Bionanocomposites through Factorial Design for Electrical Insulation Application, *Polymers*, 2024, **16**, 2117.

39 A. B. Abou Hammad, A. A. Al-esnawy, A. M. Mansour and A. M. El Nahrawy, Synthesis and characterization of chitosan-corn starch-SiO_2/silver eco-nanocomposites: exploring optoelectronic and antibacterial potential, *Int. J. Biol. Macromol.*, 2023, **249**, 126077.

40 K. Hayashida, Highly improved dielectric properties of polymer/α-Fe_2O_3 composites at elevated temperatures, *RSC Adv.*, 2016, **6**, 64871–64878.

41 Z. M. Dang, *et al.*, Fundamentals, processes and applications of high-permittivity polymer–matrix composites, *Prog. Mater. Sci.*, 2012, **57**, 660–723.

42 V. Senthil, *et al.*, Dielectric relaxation behavior and electrical conduction mechanism in polymer-ceramic composites based on Sr modified Barium Zirconium Titanate ceramic, *J. Polym. Res.*, 2012, **19**(7), 9898.

43 J. Chen, P. Jiang and X. Huang, High Dielectric Constant (High k) Polymer Composites, *Encycl. Polym. Sci. Technol.*, 2021, 1–44, DOI: 10.1002/0471440264.PST674.

44 Z. Cai, *et al.*, Dielectric response and breakdown behavior of polymer-ceramic nanocomposites: the effect of nanoparticle distribution, *Compos. Sci. Technol.*, 2017, **145**, 105–113.

45 M. Jebli, *et al.*, Structural and morphological studies, and temperature/frequency dependence of electrical conductivity of $Ba_{0.97}La_{0.02}Ti_{1-x}Nb_{4x/5}O_3$ perovskite ceramics, *RSC Adv.*, 2021, **11**, 23664–23678.

46 N. Yousf, *et al.*, Synthesis, Characterization, and Electrochemical Sensing Applications of Bimetallic Oxide/Carbon Nanomaterials Hybrids, *ECS J. Solid State Sci. Technol.*, 2021, **10**, 121005.

47 G. Praveen Kumar, *et al.*, A Facile synthesis of the Nickel Oxide Nanoparticles for the Effective Electrochemical Detection of Hydrogen peroxide in Contact Lens Solution, *Int. J. Electrochem. Sci.*, 2020, **15**, 8181–8189.

48 S. Barkaoui, M. Haddaoui, H. Dhaouadi, N. Raouafi and F. Touati, Hydrothermal synthesis of urchin-like Co_3O_4 nanostructures and their electrochemical sensing performance of H_2O_2, *J. Solid State Chem.*, 2015, **228**, 226–231.

49 Y. Zhang, *et al.*, Highly sensitive graphene-Pt nanocomposites amperometric biosensor and its application in living cell H_2O_2 detection, *Anal. Chem.*, 2014, **86**, 9459–9465.

50 A. Awais, M. Arsalan, Q. Sheng and T. Yue, A Non-enzymatic Hydrogen Peroxide Sensor with Enhanced Sensitivity Based on Pt Nanoparticles, *Anal. Sci.*, 2021, **37**, 1419–1426.

51 L. Kong, *et al.*, Interconnected 1D Co_3O_4 nanowires on reduced graphene oxide for enzymeless H_2O_2 detection, *Nano Res.*, 2015, **8**, 469–480.

52 X. Huang, Y. Zhu and E. Kianfar, Nano Biosensors: Properties, applications and electrochemical techniques, *J. Mater. Res. Technol.*, 2021, **12**, 1649–1672.

53 M. S. Hashem, H. S. Magar, A. M. Fahim and R. A. Sobh, Antioxidant-rich brilliant polymeric nanocomposites for quick and efficient non-enzymatic hydrogen peroxide sensor, *RSC Adv.*, 2024, **14**, 13142–13156.

54 H. S. Magar, M. S. Hashem and R. A. Sobh, Design of metal oxide nanoparticles-embedded polymeric nanocomposites for hydrogen peroxide chronoamperometric sensor, *Polym. Compos.*, 2024, **45**, 3653–3665.

55 A. Awais, M. Arsalan, Q. Sheng and T. Yue, A Non-enzymatic Hydrogen Peroxide Sensor with Enhanced Sensitivity Based on Pt Nanoparticles, *Anal. Sci.*, 2021, **37**, 1419–1426.

56 L. Kong, *et al.* Interconnected 1D Co_3O_4 nanowires on reduced graphene oxide for enzymeless H_2O_2 detection, *Nano Res.*, 2015, **8**, 469–480.

57 X. Huang, Y. Zhu and E. Kianfar, Nano Biosensors: Properties, applications and electrochemical techniques, *J. Mater. Res. Technol.*, 2021, **12**, 1649–1672.

58 M. S. Hashem, H. S. Magar, A. M. Fahim and R. A. Sobh, Antioxidant-rich brilliant polymeric nanocomposites for quick and efficient non-enzymatic hydrogen peroxide sensor, *RSC Adv.*, 2024, **14**, 13142–13156.

59 H. S. Magar, M. S. Hashem and R. A. Sobh, Design of metal oxide nanoparticles-embedded polymeric nanocomposites for hydrogen peroxide chronoamperometric sensor, *Polym. Compos.*, 2024, **45**, 3653–3665.